Generation of shoreward nonlinear internal waves south of the Hainan Island: SAR observations and numerical simulations

Tong Jia[1,2], Jianjun Liang[1, 3], Qiang Li[4], Jin Sha[1,3] and Xiao-Ming Li[1,3]

[1] Key Laboratory of Digital Earth Science, Aerospace Information Research Institute, Chinese Academy of Sciences, Beijing, China.

[2] University of Chinese Academy of Sciences, Beijing, China.

[3] Key Laboratory of Earth Observation of Hainan Province, Hainan Research Institute, Aerospace Information Research Institute, Chinese Academy of Sciences, Sanya, China

[4] Graduate School at Shenzhen, Tsinghua University, Shenzhen, China.

Corresponding authors: Jianjun Liang (liangjj@radi.ac.cn) and Xiao-Ming Li (lixm@radi.ac.cn)

Key Points:

- Two types of shoreward nonlinear internal waves south of the Hainan Island are identified by analyzing multiple spaceborne SAR images.
- The two types of nonlinear internal waves have different source sites and generation mechanisms.
- Background current can greatly affect the nonlinear evolution of the internal waves.

Abstract

The generation of shoreward nonlinear internal waves (NLIWs) on the continental shelf south of the Hainan Island (SHI) is investigated based on spaceborne synthetic aperture radar (SAR) observations and numerical simulations. Two types of shoreward NLIWs are identified from SAR images according to their distinct geographic distribution. One type of NLIWs, named Type-N NLIWs, is distributed on the northern SHI, and the other one is named Type-S NLIWs, distributed on the southern SHI. The SAR-observed wave occurrence frequency during the spring and neap tides, combined with the calculated body force, suggests that the Type-N NLIWs originate from the Xisha Islands, whereas the Type-S NLIWs originate from both the Xisha Islands and the continental shelf break, and the shelf break has a larger contribution. The synergistic analyses of the internal tidal ray path, gamma parameter and earliest SAR-observed NLIWs reveal that the Type-N NLIWs are excited by the impingement of the diurnal internal tidal beams emanating from the Xisha Islands on the near-surface pycnocline close to the continental shelf. Based on the realistic shelf-slope topography and tidal forcing, the two-dimensional numerical simulations using the MITgcm suggest that the Type-S NLIWs result from the nonlinear disintegration of a mode-1 diurnal internal tide which develops from a lee wave formed at the continental shelf break. Furthermore, the sensitive numerical experiments show that the background current can greatly affect the nonlinear evolution of the internal waves generated at the shelf break.

Plain Language Summary

Nonlinear internal waves (NLIWs) are large-amplitude and high-frequency gravity waves that are widely observed in the South China Sea (SCS). Previous studies mainly focus on the NLIWs in the northeastern SCS. The generation sources and mechanisms of NLIWs south of the Hainan Island (SHI) are rarely reported. The spaceborne synthetic aperture radar (SAR) is a powerful remote sensing instrument for observing NLIWs. In this paper, multiple spaceborne SAR images combined with theoretical analyses and numerical simulations were used to analyze the source sites and generation mechanisms of NLIWs in the SHI. SAR observations show that there are two types of NLIWs in the SHI. One type distributed on the northern SHI, originates from the Xisha Islands, and arises from the interaction between the diurnal internal tidal beam and the near-surface pycnocline. The other type distributed on the southern SHI, originates from both the Xisha Islands and continental shelf break. Simulations with the realistic shelf-slope topography and tidal forcing show that the NLIWs are generated by the evolution of a mode-1 diurnal internal tide. Moreover, it is found that the background current in the SHI can have a significant effect on the nonlinear evolution of internal waves.

1 Introduction

Nonlinear internal waves (NLIWs) are often observed in coastal oceans and marginal seas, and have been shown to be essential in driving interior mixing, scattering and ducting acoustic modes, and transporting materials (Apel et al., 2007; Carter et al., 2005; Chiu et al., 2004; Hosegood et al., 2004; Nazarian & Legg, 2017; Quaresma et al., 2007; Sandstrom & Elliott, 1984). Assessing these effects needs a deeply understanding of the generation and propagation processes of NLIWs. Compared with the propagation of NLIWs (Helfrich & Melville, 2006), the generation of NLIWs is more complex and receives limited investigations (Grimshaw & Helfrich, 2018; Jackson et al., 2012).

Studies have shown that the primary generation of NLIWs is attributed to the tide-topography interactions (Haury et al., 1979; Gerkema & Zimmerman, 2008). Such generation may be clarified by the normalized tidal excursion length $\delta = U_0/L\omega$ (Bell, 1975; Buijsman et al., 2010), where U_0 is the characteristic barotropic flow velocity, ω is the tidal frequency, and L is a horizontal length scale associated with the topography. When $\delta \ll 1$, internal tides at the tidal forcing frequency are mainly excited. In the regime, the internal tide may radiate from the critical point of the generation region in a form of wave beam (Cole et al., 2009; Pingree & New, 1991), propagating along the characteristic line: $dx/dz = \sqrt{(N^2 - \omega^2)/(\omega^2 - f^2)}$, where f is the Coriolis parameter and N is the buoyancy frequency. Impinging upon a moderately stratified pycnocline, the internal tidal beam can scatter into a interfacial internal wave which may subsequently disperse into NLIWs (Gerkema, 2001). The generation mechanism is called internal tidal beam mechanism. When $\delta \sim 1$, internal waves at both the forcing and harmonic frequencies are excited. Due to the frequency dispersion and dissipation, a mode-1 internal tide emerges and could transform into NLIWs under the influence of non-hydrostatic and rotational dispersion in the far field (Buijsman et al., 2010; Lee & Beardsley, 1974). The generation mechanism is called internal tide evolution mechanism. When $\delta >> 1$, an unsteady lee wave is formed at the backslope of the topography. As soon as the tidal current slackens and turns, the lee depression may move over the topography and effectively evolve into a rank-ordered NLIW packet (Maxworthy, 1979). The generation mechanism is called lee wave mechanism.

Though NLIWs propagate within the ocean interior, they can be easily detected by spaceborne synthetic aperture radar (SAR) due to the modulation of sea surface roughness by the wave-induced sea surface currents (Alpers, 1985). By analyzing SAR images, researchers have investigated the characteristic, generation and propagation of NLIWs in many parts of the world ocean, such as the northeastern South China Sea (SCS) (Liu et al., 1998; Zhao et al., 2004), the Andaman Sea (Alpers et al., 1997), the Bay of Biscay (Da Silva et al., 2007) and the White Sea (Kozlov et al., 2014). In the northwestern SCS, NLIWs have been found to exist widely on the continental shelf (Liang et al., 2019; Wang et al., 2013). The draft diagram of the NLIW distribution in the northwestern SCS, superimposed by the previous studies in this region is shown in Figure 1. These studies have presented different source sites and generation mechanisms of NLIWs. By analyzing SAR images and calculating the body force, Li et al. (2008) suggested that the SAR-observed NLIWs northeast of the Hainan Island originate from the tide-topography interactions in the Luzon Strait. By contrast, Xu et al. (2010) argued that the field measured NLIWs in the same region are caused by the disintegration of the diurnal internal tides formed at the continental shelf break. Su and Pohlmann (2009) proposed that the NLIWs east of the Hainan Island are generated by surface winds and buoyancy forcing rather than barotropic tides. Liang et al. (2019) has recently investigated the lifecycle of NLIWs southeast of the Hainan Island, and their studies revealed that the NLIWs are generated by the internal tides formed at a sill in the Xisha Islands, approximately 215 km away from the continental shelf break. For the westward NLIWs observed around 16°N close to the Vietnam coast, the remote sensing images and numerical simulations revealed that they could be generated by the mixed lee waves over sills around the Zhongsha Islands (Li et al., 2011). A recent analysis of diurnal baroclinic tidal horizontal flux suggested that these westward NLIWs might also originate from the slope south of the Hainan Island (Yan et al., 2020). Moreover, Xu et al. (2016) found that the seaward propagating NLIWs south of the Hainan Island are generated by the barotropic tidal flows interacting with the arc-like continental slope.

Scrutinizing these previous studies in the northwestern SCS, we find the detailed generation processes of shoreward NLIWs on the shelf regions south of the Hainan Island between 16.8°N and 18°N (denoted by the red rectangle in Figure 1, shorted as SHI hereafter) remain poorly understood. This study focuses on the generation of NLIWs in the SHI, where two types of shoreward NLIWs with different geographic distributions are identified from SAR images. Joint use of the SAR observation and numerical simulation reveals the main generation process of the both wave types. In addition, as the SHI features a weak anti-cyclonic cross-shelf circulation in summer (Gao et al., 2013; Shi, 2014), the effects of the background current on the evolution of internal waves are also investigated in the study.

The paper is organized as follows: In section 2, the SAR data, numerical model and methods for determining the source sites of the NLIWs are introduced. Section 3 reveals the source sites and generation processes of the two types of NLIWs observed by SAR, and the nonlinear effects induced by the background current. Discussion of the results is presented in section 4, followed by conclusions in section 5.

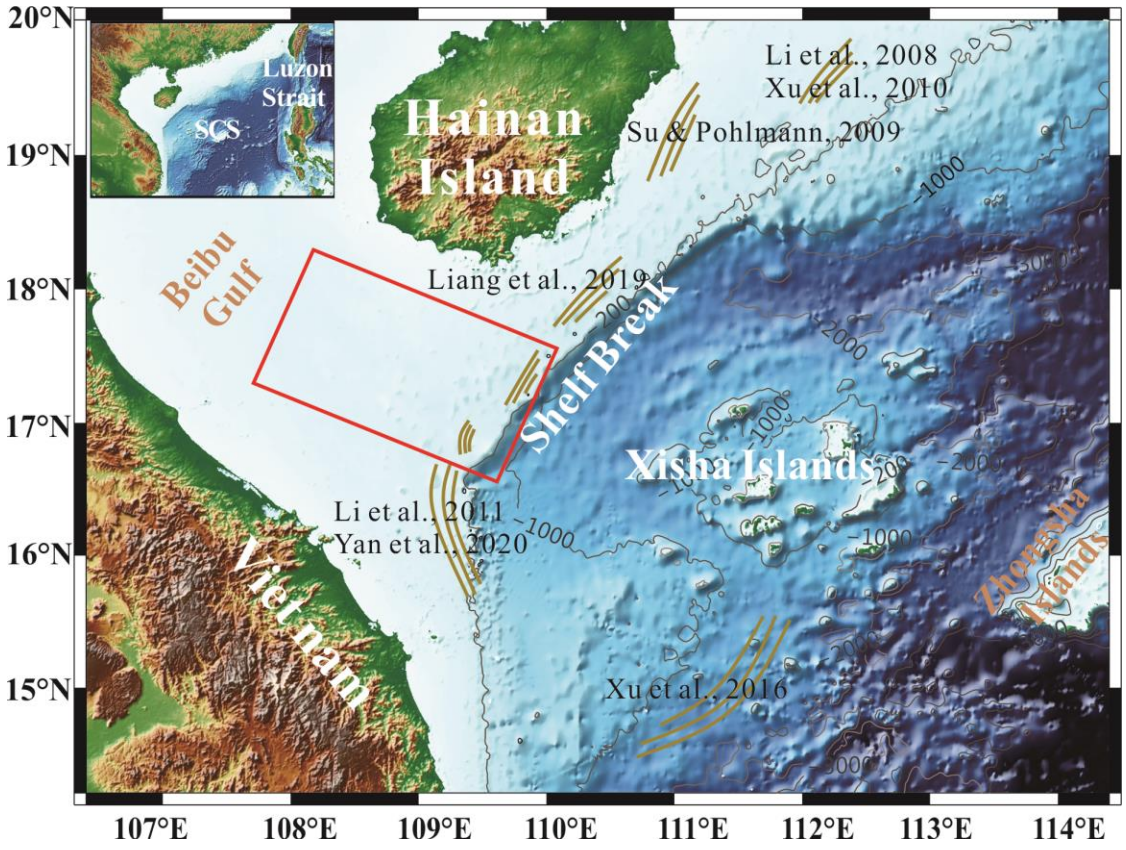

Figure 1. Draft diagram of NLIW distribution in the northwestern SCS. The brown curves indicate the distribution of NLIWs superimposed by the previous studies in black. The red rectangle indicates the area of interest in the study. The background color indicates the bottom topography, and the contour lines represent the -200 m, -1,000 m, -2,000 m, and -3,000 m isobaths.

2 Methodology

2.1 SAR data

In this paper, about 500 SAR images captured by the C-band Envisat Advanced SAR (ASAR) and L-band ALOS PALSAR between the year of 2002 and 2012 were collected to investigate the characteristics of NLIWs in the SHI. Technical specifications of the used SAR data are listed in Table 1. All the SAR data were processed by steps of radiometric calibration, refined lee filtering and geolocation.

Table 1. Technical specifications of the spaceborne SAR data acquired for the NLIW analyses

SAR	Acquisition time (year)	Imaging mode	Pixel size
Envisat ASAR	2002-2012	Wide swath mode (WSM)	75 m (WSM)
		Image precision mode (IMP)	12.5 m (IMP)
ALOS PALSAR	2006-2011	High resolution mode	6.25 m

2.2 NLIW occurrence frequency

The SAR-observed NLIW occurrence frequency during the spring and neap tides was used to conjecture the source sites of the NLIWs in the SHI. In general, the emergence of a much higher wave occurrence frequency during the spring tides suggests that the source site is at the continental shelf break, whereas the appearance of a much higher wave occurrence frequency during the neap tides indicates that the source site is at other regions (Hamann et al., 2018).

Following the calculation of monthly SAR-observed internal wave occurrence frequency presented in Zheng et al. (2007), the SAR-observed NLIW occurrence frequency related to the fortnight tidal cycle is defined as:

$$p_i = q_i \left(\frac{n_i}{\sum_{j=1}^{2} n_j} \right) \#(1)$$

where n_i (n_j) is the total number of days on which the NLIWs are imaged by SAR, $i(j) = 1$ represents the spring tidal period while $i(j) = 2$ represents the neap tidal period. The spring (neap) tidal period refers to the three days before and after the spring (neap) tide day. $q_i = D_m/D_i$ is introduced as a deweighted factor for considering the possible uneven distribution of SAR working days on the spring tidal period and neap tidal period. Here D_i is the total number of SAR working days for the spring tidal period ($i = 1$) or neap tidal period ($i = 2$), and D_m is the minimum in D_i.

2.3 Body force

Apart from the occurrence frequency related to the fortnight tidal cycle, the body force or the barotropic forcing term proposed by Baines (1982) was also employed for identifying the generation sites in the SHI. The areas with large body forces are usually sites where strong tidal currents oscillate across shallow steep bathymetry, namely, the potential internal wave generation sources.

The body force F is defined as:

$$F = zN^2(z)\int \overrightarrow{Q(x,y)}dt \cdot \nabla\left(\frac{1}{h(x,y)}\right) \#(2)$$

where x, y, z is the zonal, meridional and vertical coordinate, h is the water depth, $N(z)$ is the buoyancy frequency, $\overrightarrow{Q(x,y)} = (Q_x, Q_y) = (uh, vh)$ is the barotropic tidal volume flux vector, u and v are the zonal and meridional components of the barotropic tidal velocity, respectively.

In the calculation of the body force, the seasonal climatology temperature and salinity profiles from the World Ocean Atlas 2018 (WOA18) with a horizontal grid resolution of 0.25° at 102 standard vertical levels (0-5,500 m) were used to calculate the stratification N^2. The tidal currents were taken from the 1/30°-resolution inverse tidal model, the China Seas & Indonesia 2016 (Egbert & Erofeeva, 2002). The water depth was derived from GEBCO_2020 dataset, which is at 15" intervals in zonal and meridional direction.

2.4 Numerical model

To elucidate the generation process of NLIWs in the southern SHI, we applied the nonlinear and non-hydrostatic Massachusetts Institute of Technology general circulation model (MITgcm) in a realistic model setup to simulate the generation of the NLIWs observed on a SAR image. The MITgcm is described in detail by Marshall et al. (1997a, 1997b), and its source code and further documentation are available online (http://mitgcm.org). The simulated NLIWs (NLIW1 and NLIW2) are shown in Figure 2b.

The model was performed in a two-dimensional (X-Z) domain, with X-axis opposite to the propagation direction of the simulated waves and Z-axis directing vertically upward. The length of the model domain along the X-axis is approximately 680 km. To resolve the generation of NLIWs, the horizontal grid resolution was set to 25 m in the main model part, telescoped to reach a maximum of 5.025 km at the model boundaries. The time step was set to 4 s to satisfy the Courant-Friedrichs Lewy condition. In the Z-axis, a total of 125 layers were used: upper 60 layers with 5-m resolution, following 30 layers with 10-m resolution and another 30 layers with 20-m resolution, and the bottom 5 layers with 40-m resolution. The Richardson number-dependent parameterizations of turbulent closure (Pacanowski & Philander, 1981) were used to calculate the vertical viscosity $\upsilon = \frac{\upsilon_0}{(1+\alpha Ri)^n} + \upsilon_b$ and vertical diffusivity $\kappa = \frac{\upsilon}{1+\alpha Ri} + \kappa_b$, where $Ri = N^2(z)/(u_z^2 + v_z^2)$ is the Richardson number, $u(\upsilon)$ is zonal (meridional) velocity. The background viscosity $\upsilon_b = 1.0 \times 10^{-5}\ m^2 s^{-1}$, background diffusivity $\kappa_b = 1.0 \times 10^{-5}\ m^2 s^{-1}$, $\alpha = 5$, $n = 1$, and $\upsilon_0 = 1.0 \times 10^{-1}\ m^2 s^{-1}$. The horizontal viscosity and diffusivity were set as $10^{-2}\ m^2 s^{-1}$ and $10^{-5}\ m^2 s^{-1}$, respectively.

The bathymetry used in the model was extracted from GEBCO_2020 dataset. To specify the bathymetry profile along the propagation direction of the simulated waves, an average on the bathymetry of multiple sections (marked by the black rectangle in Figure 2a) across the simulated waves was made. Then the averaged bathymetry was set to -101.1 m west and -1,314 m east. The final bathymetry profile used in model is indicated by the red line in Figure 2c.

The initial stratification in the model was set to be horizontally uniform, and its data were taken from a SCS physical oceanographic dataset-SCSPOD14 (Zeng et al., 2016) for August (the acquisition month of NLIW1 and NLIW2). The SCSPOD14 has a horizontal resolution of 0.25° at 57 standard vertical levels (0-1,500 m). Figure 3 shows the mean temperature, salinity, and

buoyancy frequency profiles acquired from the SCSPOD14 during August around the southern SHI.

The model was initialized from rest and was driven by a 4-day time series of the barotropic tidal velocities with/without the background current at its boundaries. The tidal forcing was constructed from the tidal model of China Seas & Indonesia 2016 during the period from August 20, 2011 to August 24, 2011, and projected to the propagation direction of the simulated waves. The background current was acquired from the 3-hourly Hybrid Coordinate Ocean Model (HYCOM) reanalysis data from August 16, 2011 to August 23, 2011 in the southern SHI. A 7-day average was firstly applied to the HYCOM data, after which a vertical uniform background current was calculated according to the calculation of barotropic velocity by Li (2014). The background current was also projected to the cross-wave direction. Additionally, a 137.75 km wide (over 32 cells) sponge layer following Lavelle and Thacker (2008) which was also adopted by Buijsman et al. (2014) and Liang et al. (2019) was imposed at model boundaries, to allow for the inward propagation of the tidal barotropic waves while damping the outward-propagating baroclinic waves.

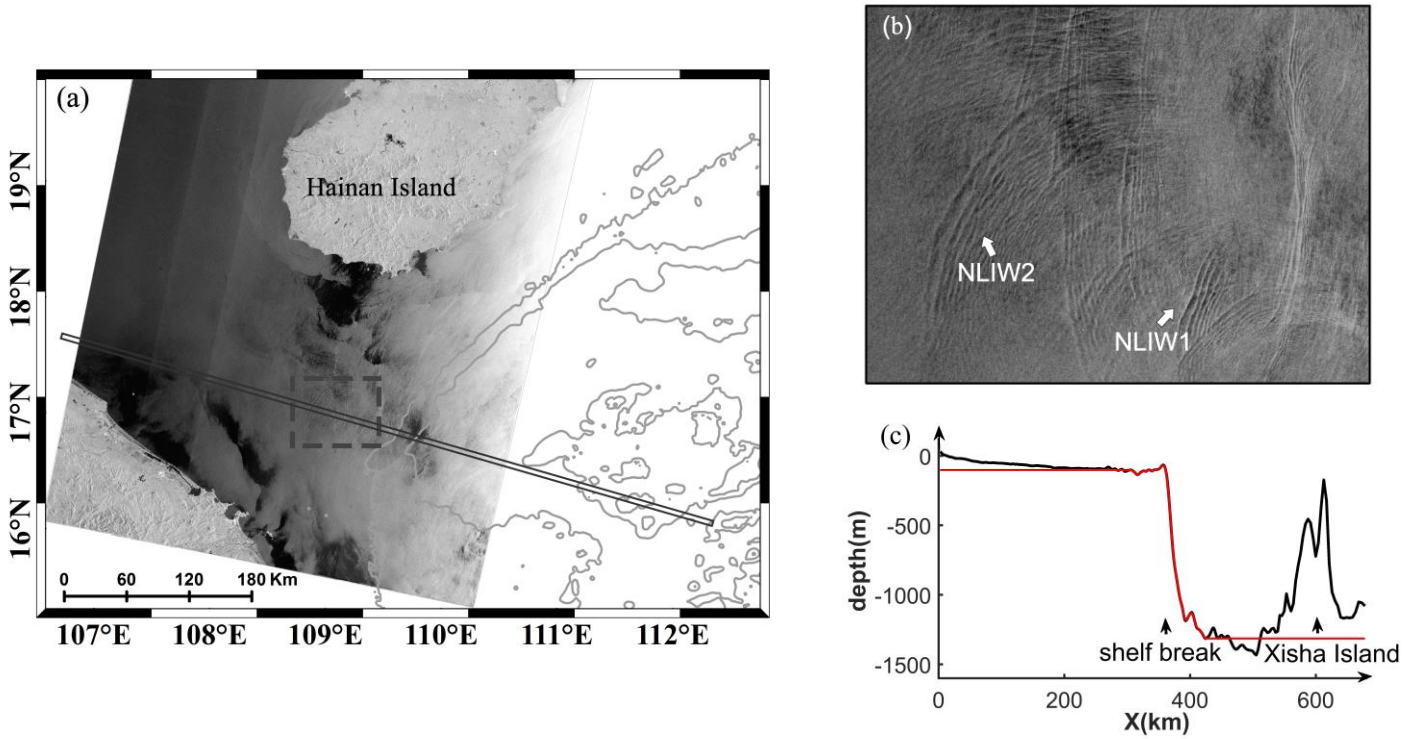

Figure 2. (a) A subset of an Envisat ASAR image acquired on August 23, 2011 (02:41 UTC) showing the surface signature of NLIW1 and NLIW2. (b) Closeup of the fragment depicted by the black dashed box of panel (a). (c) Averaged topography calculated in the black rectangle of panel (a). The section along the red line is used for the numerical simulation.

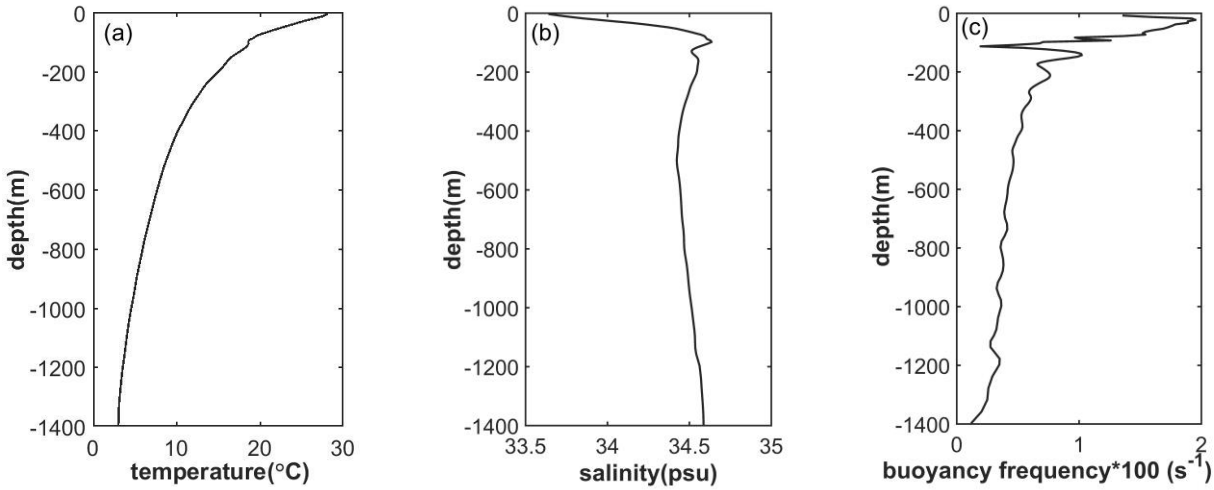

Figure 3. Initial (a) temperature, (b) salinity and (c) buoyancy frequency of the model in August derived from the SCSPOD14.

3 Results

3.1 SAR observations of two types of NLIWs

About 90 groups of shoreward NLIW packets were identified on the continental shelf of the SHI from the collected ASAR and PALSAR images. The leading crests of these NLIWs were depicted to map the spatial distribution of NLIWs in the SHI (Figure 4). Most of the NLIWs have a leading crest of tens of kilometers long, and travel in the southeast-northwest direction onto the Beibu Gulf. Moreover, the geographic distribution of these observed NLIWs in the SHI is separated into a northern part (blue curves, Figure 4) and a southern part (red curves, Figure 4). Sometimes the NLIWs in the northern and southern SHI meet each other and produce the wave-wave interactions as shown in Figure 5. The distinct feature regarding the geographic distribution suggests that there are two types of NLIWs, possibly relating to different generation sites. We term the NLIWs north of the SHI as Type-N NLIWs, while these NLIWs south of the SHI are termed as Type-S NLIWs. In the SHI, about 45 (33) groups of Type-N (Type-S) NLIWs are observed. In addition to the Type-N and Type-S NLIWs, there are a few peculiar NLIWs in the SHI that are colored in black in Figure 4. These waves are rarely observed, and either extend more than 100 km spanning the whole SHI region or travel onshore obliquely to the isobaths in east-west direction. We do not consider these waves in the study.

This paper aims to investigate the source sites and generation mechanisms of the frequently observed Type-N and Type-S NLIWs in the SHI region. Previous studies have suggested that the Xisha Islands, continental shelf break, Zhongsha Islands and Luzon Strait are the potential source sites for the NLIWs in the northwestern SCS. However, for the Type-N and Type-S NLIWs, the Zhongsha Islands are not considered as the source site, because the Xisha Islands are located on the pathway of the northwestward baroclinic tidal energy radiating from the Zhongsha Islands. These northwestward baroclinic tides would be mostly refracted or diffracted by the Xisha Islands to southward, rather onto the continental shelf (Yan et al., 2020). Similarly, the Luzon Strait is also not regarded as an efficient source site for the Type-N and

255 Type-S NLIWs, because the diurnal internal tides radiating from the Luzon Strait primarily
256 refract southwestward to the equator due to the earth's rotation and probably cannot refract
257 northwestward onto the continental shelf of the SHI (Zhao, 2014). Moreover, the patterns of the
258 wave crests appearing near the shelf break (Figure 4) do not support the Luzon Strait as the
259 source site. Therefore, the following analysis is to clarify whether the Type-N and Type-S
260 NLIWs originate from the Xisha Islands, the continental shelf break or the both.

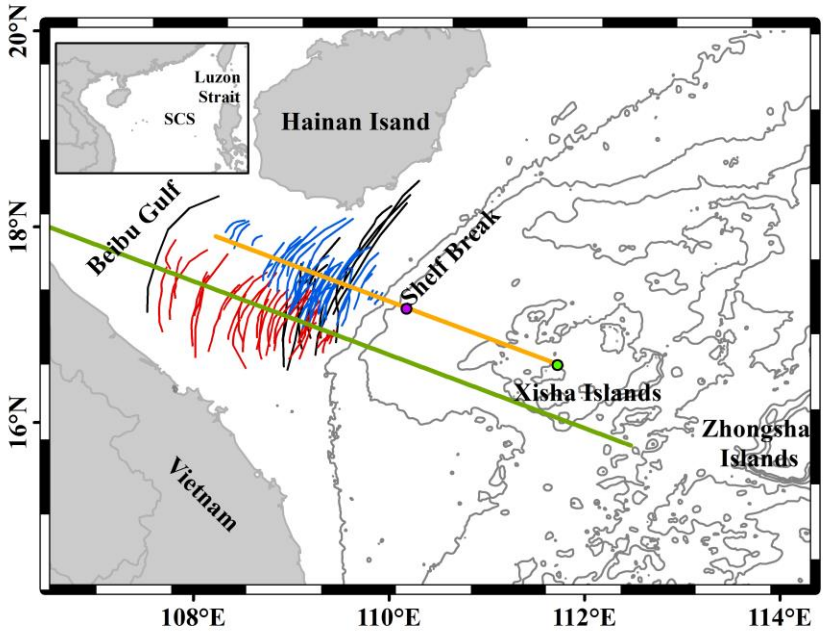

261

262 **Figure 4.** Distribution map of the NLIWs in the SHI detected in the Envisat ASAR and ALOS
263 PALSAR images in period of 2002-2012. The main waves of Type-N NLIWs (Type-S NLIWs)
264 distributed on the northern (southern) part of SHI are shown in blue (red) curves while the
265 remaining less observed waves in the SHI are indicated in black curves. The orange straight line
266 passing through the Xisha Islands denotes the section taken for the ray path estimation of Type-
267 N NLIWs, while the green straight line denotes the section taken for the numerical simulation of
268 Type-S NLIWs. The green and purple points denote the critical point (16.60°N, 111.72°E) and
269 the resurfacing point (17.14°N, 110.17°E) along the ray path, respectively. The grey curves
270 indicate the depth contours of -200 m, -1,000 m, -2,000 m and -3,000 m.

271

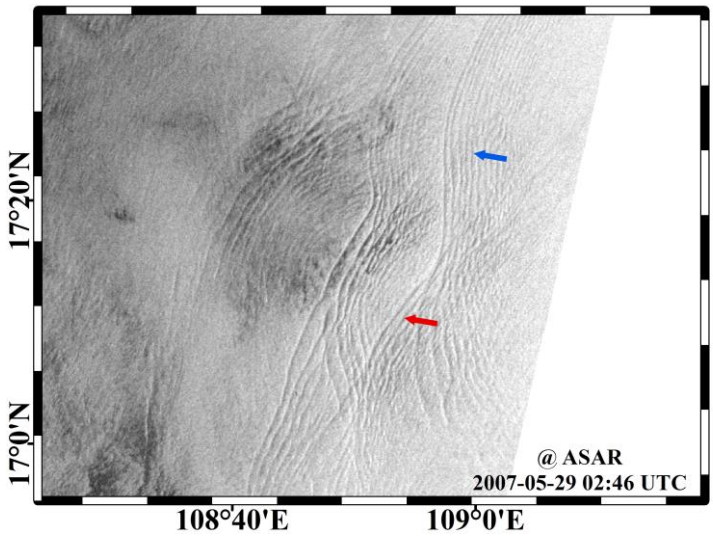

Figure 5. A typical example of SAR images showing that the NLIWs separately distributed on the northern part (denoted by the blue arrows) and the southern part (denoted by the red arrows) of the SHI meet each other.

3.2 Generation of the Type-N NLIWs

3.2.1 Source site

Based on the collected ENVISAT ASAR and ALOS PALSAR data in the SHI, we investigated the source site of the Type-N NLIWs by analyzing the body force and the SAR-observed occurrence frequency related to the fortnight tidal cycle.

Figure 6 shows the distribution of the body force for the K_1, O_1 and M_2 constituents in summer, since the summer is the season when the NLIWs are commonly observed to occur frequently (Huang et al., 2008; Jia et al., 2018). The M_2 tidal forcing is rather weak and thus cannot generate NLIWs, while the diurnal tidal forcing is strong and is concentrated along the continental shelf break and around the Xisha Islands. Furthermore, the diurnal tidal forcing along the shelf break close to the Type-N NLIWs is comparable to that around the Xisha Islands, implying that both the shelf break and the Xisha Islands are the possible source sites of the Type-N NLIWs. However, the statistical results of the SAR-observed occurrence frequency (Table 2) show that the Type-N NLIWs mostly occur during the neap tidal period, ruling out the shelf break as the primary source site of the Type-N NLIWs. Consequently, the Type-N NLIWs mainly originate from the Xisha Islands.

Table 2. Statistical results of SAR-observed Type-N NLIW occurrence frequency related to the fortnight tidal cycle

Type-N NLIW	Spring tidal period	Neap tidal period
SAR working days	122	131
NLIW imaged days	9	18
Occurrence frequency	33.33%	62.09%

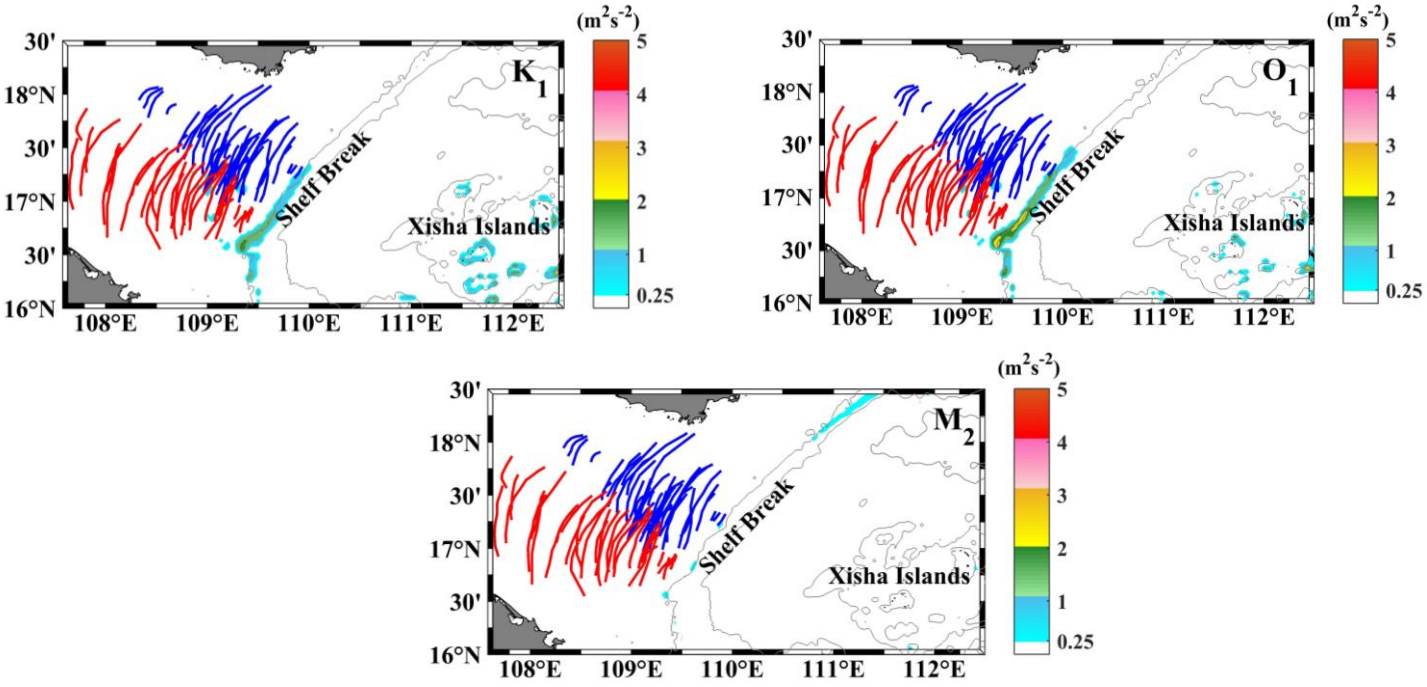

Figure 6. Distribution of the maximum depth-integrated body force for the K_1, O_1 and M_2 constituents in summer. The blue curves indicate the Type-N NLIWs while the red curves indicate the Type-S NLIWs. The grey curves indicate the depth contours of -200 m, -1,000 m, -2,000 m and -3,000 m.

3.2.2 Internal tidal beam mechanism

The NLIW occurrence frequency and body force estimation have revealed that the Xisha Islands are the major source site for the Type-N NLIWs. The subsequent arising question is how the internal tide sourcing from the Xisha Islands transits the deep basin for over 200 km and evolves into the Type-N NLIWs on continental shelf regions. In this section, we use some theoretical analyses combined with the SAR observations to answer this question.

On the one hand, the tidal excursion length of the ridge in the Xisha Islands is around 0.025, suggesting that the Xisha Islands are in the linear internal tide regime. On the other hand, the crest of the ridge is at depth of -124 m that is below the pycnocline, suggesting that the tide-topography interaction at the Xisha Islands occurs within an approximately uniform stratification. The two aspects combined with the critical topography favor to generate an internal tidal beam at the ridge. To depict the baroclinic energy radiating process, we determined the ray paths of the diurnal internal tide, emanating from the critical point of the ridge slope on the section along the main wave propagation direction. The section is depicted in Figure 4. The ray path was computed with the mean summer stratification from WOA18. As found, the ray path firstly emanates from the critical point (16.60°N, 111.72°E, denoted by the green point in Figures 4 and 7) at the ridge. Then it slopes downward into the deep ocean. After reflection from the bottom, it returns to the surface at the point (17.14°N, 110.17°E, denoted by the purple point in Figures 4 and 7) where it hits the seasonal pycnocline over the -1187-m isobath near the continental shelf region. Gerkema (2001) proposed a gamma (γ) parameter to characterize the local stratification conditions supporting the internal wave generation after the internal tidal

beam impinging on the pycnocline. For γ either very small or very large, there is no significant transfer of energy from beams to interfacial waves. At the resurfacing point of northern SHI, the parameter γ is approximately 0.15. This value is rather close to the optimum regime ($\gamma = 0.12$, as defined in Gerkema, 2001) for generating internal waves. In other words, the beam from the Xisha Islands intersecting with the pycnocline is very likely to give rise to the interfacial wave. As the interfacial wave propagating along the pycnocline approaches the shelf break, the abrupt shoaling bottom topography can strengthen its nonlinearity. Thus, the interfacial wave can efficiently disintegrate into NLIWs near the shelf break. Figure 8 shows the earliest observed Type-N NLIWs on SAR images, locating only about 4 km west of the shelf break (see Figure 7), which provides evidence for the tidal beam generation mechanism of the Type-N NLIWs.

In summary, the ray path analysis, as well as the γ parameter calculation together with the earliest SAR-observed Type-N NLIWs, support the generation process of Type-N NLIWs as follows: the internal tide emanating from the Xisha Islands transits the deep basin in the form of the tidal beam, undergoes reflection from the sea bottom and then intersects with the pycnocline near the continental shelf region to give rise to the interfacial wave, which finally nonlinearly transforms into the NLIWs close to the shelf break.

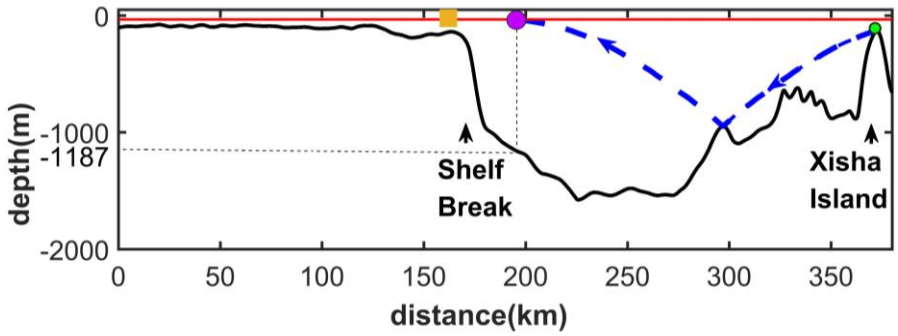

Figure 7. Diagram of the diurnal internal tidal ray path for the section marked in Figure 4. The black line denotes the topography variations along the section. The blue line with arrow denotes the propagation of internal tidal energy along the ray. The red line denotes the pycnocline. The orange, purple and green points denote the locations of earliest SAR-observed Type-N NLIWs, resurfacing point (17.14°N, 110.17°E) and critical point (16.60°N, 111.72°E), respectively.

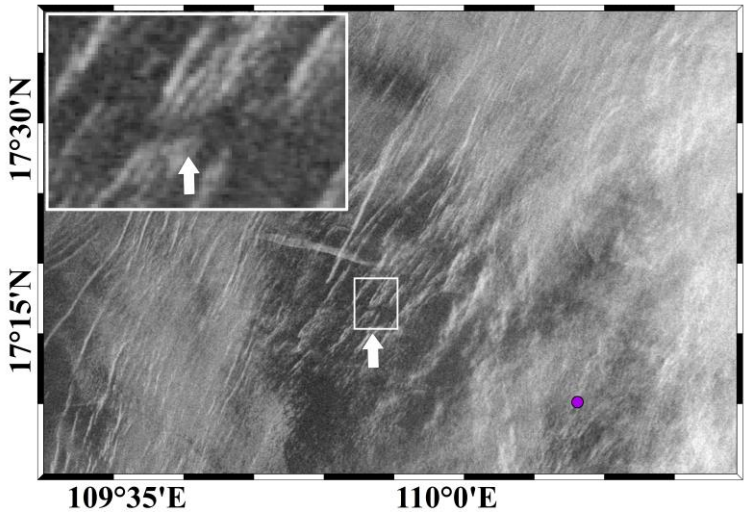

Figure 8. A subset of an Envisat ASAR image acquired on 26 May 2007 at 02:40 UTC showing a packet of earliest observed Type-N NLIWs (see inset). The purple point denotes the resurfacing point (17.14°N, 110.17°E).

3.3 Generation of the Type-S NLIWs

3.3.1 Source site

Similar to the Type-N NLIWs, the body force and the wave occurrence frequency were also estimated to determine the source site of the Type-S NLIWs.

The wave occurrence frequency of Types-S NLIWs (Table 3) is much different from that of Type-N NLIWs which have a much larger occurrence frequency in the neap tidal period (Table 2). For the Type-S NLIWs, the occurrence frequency in the spring tidal period is comparable with that in the neap tidal period, and even a higher occurrence frequency resides in the spring tidal period. The statistical results suggest that both the Xisha Islands and the continental shelf break are the source sites of the Type-S NLIWs, and the shelf break seems to contribute more to generate the Type-S NLIWs. Moreover, the diurnal tidal forcing along the shelf break close to the Type-S NLIWs (Figure 6) is also stronger than that around the Xisha Islands, further indicating that the shelf break plays a more important role in generating the Type-S NLIWs compared to the Xisha Islands. Hence, we performed a two-dimensional (2D) numerical simulation with the MITgcm to examine the role of the shelf break in generating the Type-S NLIWs.

Table 3. Statistical results of SAR-observed Type-S NLIW occurrence frequency related to the fortnight tidal cycle

Type-S NLIW	Spring tidal period	Neap tidal period
SAR working days	99	112
NLIW imaged days	10	9
Occurrence frequency	52.63%	41.87%

3.3.2 Role of shelf break

The 2D numerical model was set with nearly realistic ocean environment to reproduce the generation process of the Type-S NLIWs observed on a SAR image, i.e., the NLIW1 and NLIW2 shown in Figure 2b. Details of the model setup can refer to the section 2.4.

The time for the SAR observation is referred to T. Figure 9 displays the spatial-temporal structure of 25.5 isotherms (representing the thermocline) during the time span T-42 hours to T+14 hours. We note that a lee wave IWB (marked in red arrow lines, Figure 9) between T-42 hours and T-34 hours develops on the east (lee side) of the shelf break during and immediately after the maximum eastward flow. Scrutinizing the wave field around the shelf break (Figure 10a) shows that the amplitude of the lee wave can achieve tens of meters. As soon as the eastward current slackens and turns to the west, the lee wave is released upstream (westward). Then a mode-1 internal tide (Figure 10b) emerges from the lee wave, steepens and produces a packet of NLIWs on its front. A similar process (marked in blue arrow lines, Figure 9) recurs near the shelf break about one diurnal period after the IWB generation. The new generated internal wave is labelled as IWA. Thus, the simulation results demonstrate that the shelf break can trigger NLIWs by internal tide evolution mechanism.

At time T, the simulated internal waves IWA and IWB are correspondingly close to the SAR observed NLIW1 and NLIW2. The overall match confirms the continental shelf break as a generation source and reveals the internal tide evolution mechanism for the Type-S NLIWs. However, there are some slight discrepancy in wave patterns between the simulated and SAR observed waves. On SAR images, NLIW1 and NLIW2 manifest as the well-developed nonlinear wave packets. In the simulation, IWB is consistent with the SAR observation and has also evolved into the well-developed NLIWs at time T (see Figure 10c). But IWA still appears in the form of the internal tide at time T, whose front does not steepen and disperse into NLIWs until the time of T+8 hours. Because the SHI features an anti-cyclonic cross-shelf circulation in summer (Gao et al., 2013; Shi, 2014), the weak nonlinearity of IWA is expected to be caused by the absence of the background current in the present simulation. Hence, the background current is added into the model in the next section, whose effects on the Type-S NLIWs are thereafter investigated.

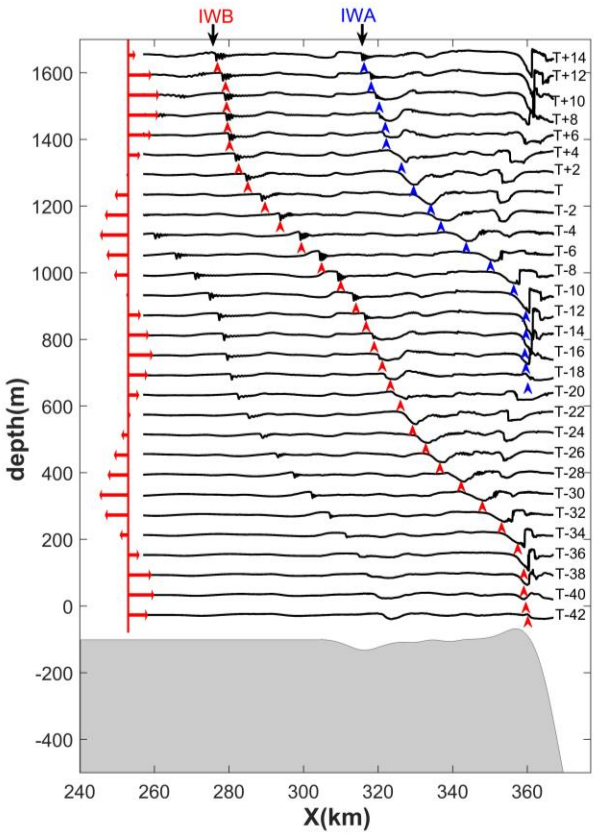

399 **Figure 9.** Horizontal profiles of 25.5℃ isotherms taken with a 2-hour interval from 42 hours
400 before T (ASAR acquisition time) to 14 hours after T in the simulation. The grey area indicates
401 the bottom topography used in the model. The black horizontal lines indicate the 25.5℃
402 isotherms, whose depth depicted on the vertical axis are lifted using the formula: $h(j) +$
403 $\left(j - (T - 42)\right) * 30m$, where $h(j)$ is the realistic water depth corresponding to the 25.5℃
404 isotherm at time j. The blue and red vertical arrows follow two different wave trains IWA and
405 IWB while the red horizontal arrows at 253 km correspond to the strength of the barotropic flow
406 at IWB.
407

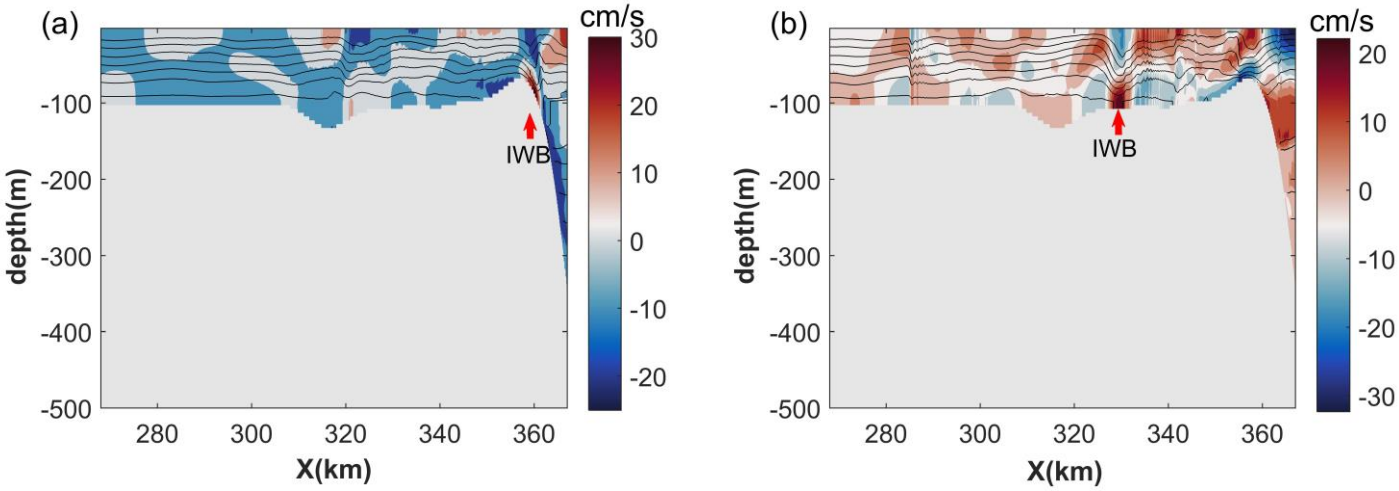

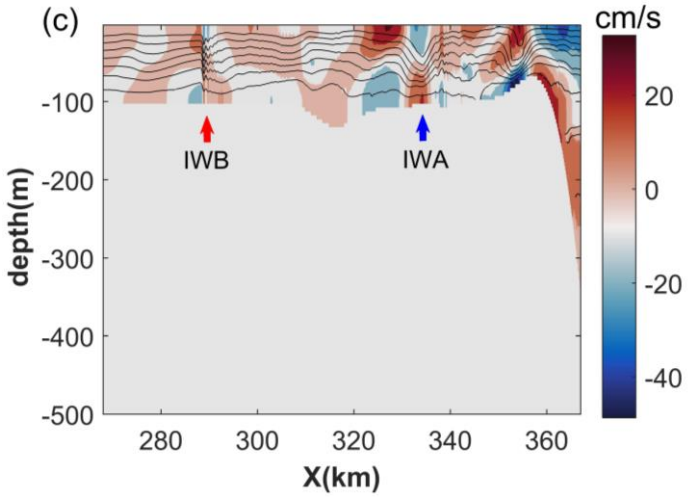

Figure 10. Numerical simulations of the baroclinic horizontal velocity field overlain with isotherms taken at time T-40 hours (a), T-22 hours (b) and T (c). Shaded color represents the horizontal baroclinic velocities, and black lines represent contour plots of temperature. Blue and red vertical arrows point to the modeled internal waves IWA and IWB, respectively. Positive velocity indicates flow to the southeast.

3.3.3 Effects of background current

Figure 11 presents the variation of the background current along the wave propagation direction, obtained from the HYCOM reanalysis data. The background current from the shelf break to the NLIW1 observation site was offshore with a magnitude of about 5 cm/s, while from the NLIW1 observation site to the NLIW2 observation site, the background current was onshore ranging from 0 to -8 cm/s. The background current cannot be neglected compared with the tidal currents of this region (about 10-35 cm/s). Given the large difference in wave nonlinearity between the NLIW1 and modeled IWA in the previous simulation, a uniform offshore background current with 0.5 cm/s at -1,000 m depth equivalently representing the realistic background current for NLIW1 is added to the 2D numerical model. Other model setups, such as the topography, stratification, tidal forcing, and grid resolution, remain the same as those in the previous simulation. The results of the new simulation experiment are plotted in Figures 12 and 13.

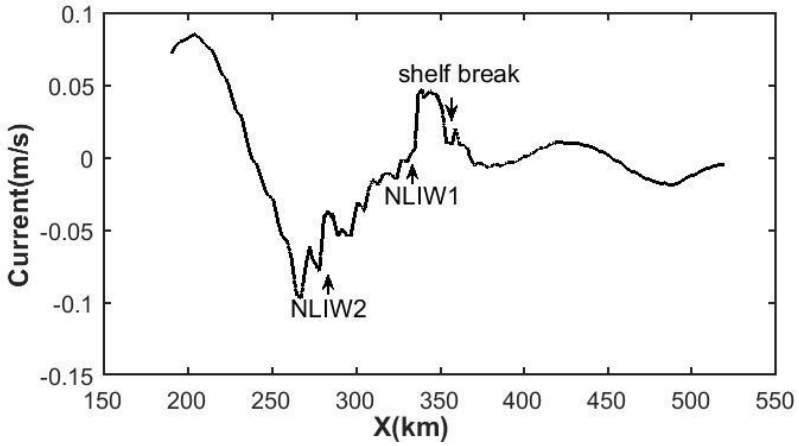

Figure 11. Variation of the 7-day averaged and vertical uniform background current along the wave propagation direction acquired from the HYCOM reanalysis data. Positive velocity indicates flow to the southeast.

The generation process of NLIWs in the new simulation is similar to that without considering the background current. So, the added offshore background current does not significantly change the generation mechanism of NLIWs, whereas it evidently changes the evolution of internal waves. With the presence of the offshore background current, IWA has evolved into an internal bore at time T which is experiencing the nonlinear disintegration on its front. Recalling that IWA was still in the form of the internal tide at time T in the previous simulation, we see that the added offshore background current increases the nonlinearity of the westward internal waves. With the reinforced nonlinearity, IWA transforms into nonlinear wave trains at the time of T+4 hours, shorter than the time of T+8 hours in the case without background current. Similar to the modeled IWA, the nonlinearity of the modeled IWB is intensified as well, which can be seen from its increased wave number and amplitude.

In summary, with or without the presence of the offshore background current, the interaction between the tidal currents and the shelf break can generate the Type-S NLIWs through the internal tide evolution mechanism. However, the background current can greatly change the nonlinear evolution of internal waves and the consequent appearance of Type-S NLIWs.

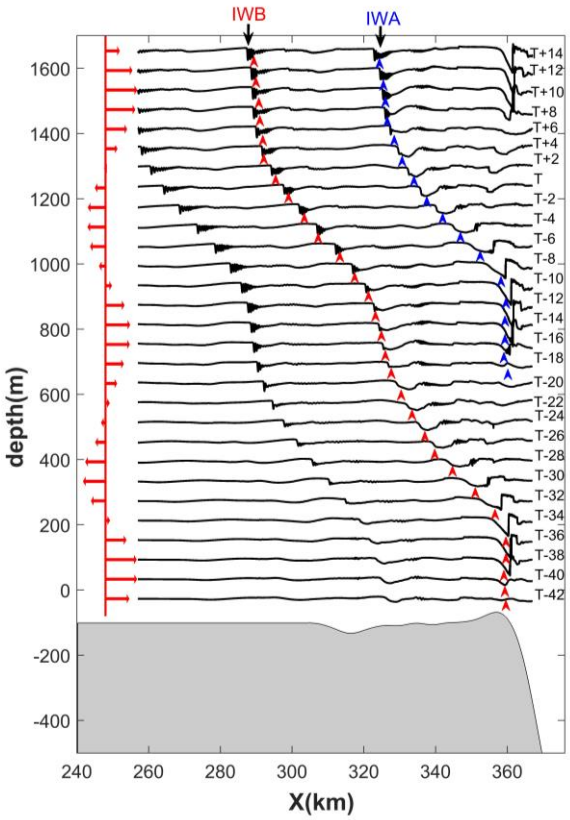

447 **Figure 12.** Horizontal profiles of the 25.5℃ isotherm taken with a 2-hour interval from 42 hours
448 before T (ASAR acquisition time) to 14 hours after T in the simulation considering the offshore
449 background current.
450

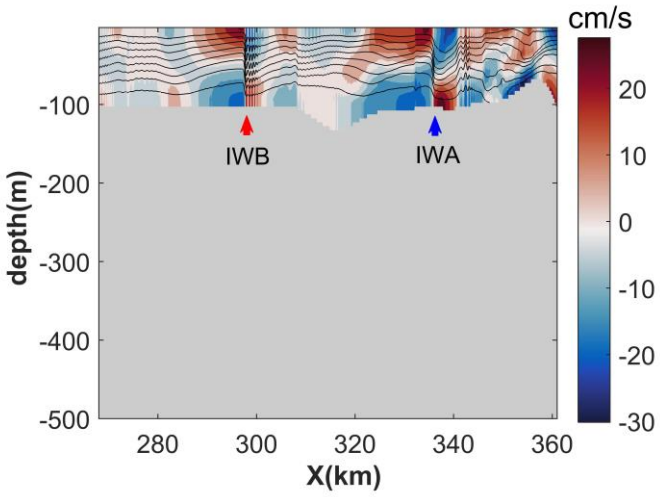

451 **Figure 13.** Numerical simulations of the baroclinic horizontal velocity field overlain with
452 isotherms taken at time T in the simulation considering the offshore background current.

4 Discussion

SAR has been widely used to investigate the generation of NLIWs in the isolated topography such as some straits (Zhao et al., 2004) and ridges (Da Silva et al., 2015). In such regions, the generation of NLIWs is coherent with the strength of internal tides which are phase-locked to local surface tide. However, many continental shelves among the world oceans are influenced by not only the local internal tides but also the incident internal tides, such as the New Jersey shelf (Nash et al., 2012) and Portuguese shelf (Sherwin et al., 2002). The multiple potential baroclinic energy sources make the observed internal wave field much complicated and the study of wave generation difficult. Here, we use decadal SAR data to clarify one such wave field of northwestern SCS (Figure 4), and preliminarily illustrate the individual effects of local and incident internal tides after using the SAR data determining the primary wave generation source (Tables 2 and 3). This application of SAR can be similarly applied to other continental shelves which may also have other source sites in addition to the local shelf break.

The generation of NLIWs on the continental shelves is commonly attributed to the internal tide evolution mechanism or lee wave mechanism. Here, we give the first evidence that the NLIWs on the continental shelves arise from the internal tidal beam mechanism. The internal tidal beam is formed at the Xisha Islands, which also has been found in Liang et al. (2019). The internal tidal beam scatters into an interfacial internal wave on the continental slope within the moderately stratified pycnocline. The interfacial internal wave further transforms into Type-N NLIWs at the edge of the continental shelf break under the influence of the pycnocline and the abruptly shoaling topography (Figure 7). Whether the generation mechanism is also applied to other exposed continental shelves requires further study, and how much of the beam energy transferred to the interfacial internal waves also remains to be clarified, since the question maybe also relevant to the global internal tide dissipation (Akylas et al., 2007).

The generation of the Type-S NLIWs is much more complex than that of the Type-N NLIWs, because the nearly equal SAR-observed occurrence frequency (Table 3) suggests that the Type-S NLIWs are produced by a combined effort of local and incident internal tides. The incident internal tide, coming from the Xisha Islands, can interfere with the local internal tide generated at the continental shelf break, and thus affect the generation of the Type-S NLIWs (Kelly & Nash, 2010). However, the incident internal tide has not been considered in the present study, which could be a primary reason that the modeled IWA is still not well formed at the SAR observation time (Figure 13).

In addition to the effects of the incident internal tides, a sheared background current exists in the shelf region (Figure 11). The current is not occasional and is associated with an anti-cyclonic cross-shelf circulation (Gao et al., 2013; Shi, 2014). However, the effects of the background current on the generation of NLIWs remain unknown. In the study, we make a first step to add a horizontal and vertical uniform background current in the 2D numerical model. The model shows that the current greatly changes the evolution process of internal waves and reduces the occurrence time of SAR-observed NLIWs by 4 hours. Given the strong horizontal and vertical shear of background currents, a field measurement (Hamann et al., 2018) is necessary in the future to clarify how the current shear affects the generation and evolution of internal waves.

5 Conclusions

The continental shelves usually have complex NLIW fields due to multiple source sites and complicated background environment. Thus, it is difficult to clarify the wave fields of the continental shelves and associated generation mechanisms. Considering the SAR is an efficient tool in investigating NLIWs, we used multiple SAR observations and numerical simulations to reveal the generation of NLIWs on the continental shelf of the SHI. Overall, two types of NLIWs with different geographic distribution are identified, referred to as Type-N and Type-S NLIWs, respectively. The Type-N NLIWs originate from the Xisha Islands and are generated by the internal tidal beam mechanism. The Type-S NLIWs originate from both the Xisha Islands and the continental shelf break, and the shelf break has a greater contribution to the wave generation. Simulations with the realistic shelf-slope topography and tidal forcing show a comparative agreement with the SAR observation, and thus reveal that the Type-S NLIWs are generated by the internal tide evolution mechanism. Additionally, the background current induced by the anti-cyclonic cross-shelf circulation in the region can greatly affect the nonlinear evolution of internal waves.

The interference of internal tides generated at the continental shelf break and the Xisha Islands will require further study by conducting the three-dimensional (3D) numerical simulations in the future.

Acknowledgments

The authors would like to thank ESA for the ENVISAT ASAR data and ALOS PALSAR data. The MODIS data were downloaded from https://ladsweb.modaps.eosdis.nasa.gov/search/, the HYCOM were downloaded from http://hycom.org/, the WOA18 data were downloaded from https://www.nodc.noaa.gov/OC5/woa18/, the SCSPOD14 data were downloaded from http://dx.doi.org/10.6084/m9.figshare.c.1513842, the GEBCO_2020 data were downloaded from https://www.gebco.net/data_and_products/gridded_bathymetry_data/, and the TPXO tidal solutions were downloaded from http://people.oregonstate.edu/~erofeevs/. The study was supported by grants from the National Science Foundation of China project (41876201, 41976001 and 91958102) and National Natural Science Fund for Distinguished Young Scholars (42025605).

References

Akylas, T. R., Grimshaw, R. H. J., Clarke, S. R., & Tabaei, A. (2007). Reflecting tidal wave beams and local generation of solitary waves in the ocean thermocline. *Journal of Fluid Mechanics, 593*, 297-313. doi:10.1017/S0022112007008786

Alpers, W. (1985). Theory of radar imaging of internal waves. *Nature, 314*(6008), 245-247.

Alpers, W., Wang-Chen, H., & Hock, L. (1997). Observation of internal waves in the Andaman Sea by ERS SAR. Paper presented at 1997 International Geoscience and Remote Sensing Symposium (IGARSS 97) on Remote Sensing-A Scientific Vision for Sustainable Development, Singapore.

532 Apel, J. R., Ostrovsky, L. A., Stepanyants, Y. A., & Lynch, J. F. (2007). Internal solitons in the
533 ocean and their effect on underwater sound. *Journal of the Acoustical Society of America*,
534 *121*(2), 695-722. doi:10.1121/1.2395914

535 Baines, P. G. (1982). On internal tide generation models. *Deep Sea Research Part A-*
536 *Oceanographic Research Papers*, *29*(3), 307-338. doi:10.1016/0198-0149(82)90098-X

537 Bell, T. H. (1975). Lee waves in stratified flows with simple harmonic time dependence. *Journal*
538 *of Fluid Mechanics*, *67*, 705-722. doi:10.1017/S0022112075000560

539 Buijsman, M. C., Kanarska, Y., & McWilliams, J. C. (2010). On the generation and evolution of
540 nonlinear internal waves in the South China Sea. *Journal of Geophysical Research: Oceans*,
541 *115*. doi:10.1029/2009JC005275

542 Buijsman, M. C., Klymak, J. M., Legg, S., Alford, M. H., Farmer, D., MacKinnon, J. A., et al.
543 (2014). Three-dimensional double-ridge internal tide resonance in Luzon Strait. *Journal of*
544 *Physical Oceanography*, *44*(3), 850-869. doi:10.1175/JPO-D-13-024.1

545 Carter, G. S., Gregg, M. C., & Lien, R. C. (2005). Internal waves, solitary-like waves, and
546 mixing on the Monterey Bay shelf. *Continental Shelf Research*, *25*(12-13), 1499-1520.
547 doi:10.1016/j.csr.2005.04.011

548 Chiu, C. S., Ramp, S. R., Miller, C. W., Lynch, J. F., Duda, T. F., & Tang, T. Y. (2004).
549 Acoustic intensity fluctuations induced by South China Sea internal tides and solitons. *IEEE*
550 *Journal of Oceanic Engineering*, *29*(4), 1249-1263. doi:10.1109/JOE.2004.834173

551 Cole, S. T., Rudnick, D. L., Hodges, B. A., & Martin, J. P. (2009). Observations of tidal internal
552 wave beams at Kauai Channel, Hawaii. *Journal of Physical Oceanography*, *39*(2), 421-436.
553 doi:10.1175/2008JPO3937.1

554 Da Silva, J. C., New, A. L., & Azevedo, A. (2007). On the role of SAR for observing "local
555 generation" of internal solitary waves off the Iberian Peninsula. *Canadian Journal of*
556 *Remote Sensing*, *33*(5), 388-403. doi:10.5589/m07-041

557 Da Silva, J. C. B., Buijsman, M. C., & Magalhaes, J. M. (2015). Internal waves on the upstream
558 side of a large sill of the Mascarene Ridge: A comprehensive view of their generation
559 mechanisms and evolution. *Deep Sea Research Part I: Oceanographic Research Papers*, *99*,
560 87-104. doi:10.1016/j.dsr.2015.01.002

561 Egbert, G. D., & Erofeeva, S. Y. (2002). Efficient inverse modeling of barotropic ocean tides.
562 *Journal of Atmospheric and Oceanic technology*, *19*(2), 183-204. doi:10.1175/1520-
563 0426(2002)019<0183:EIMOBO>2.0.CO;2

564 Gao, J., Xue, H., Chai, F., & Shi, M. (2013). Modeling the circulation in the gulf of Tonkin,
565 South China Sea. *Ocean Dynamics*, *63*(8), 979-993. doi:10.1007/s10236-013-0636-y

566 Gerkema, T. (2001). Internal and interfacial tides: beam scattering and local generation of
567 solitary waves. *Journal of Marine Research*, *59*(2), 227-255.
568 doi:10.1357/002224001762882646

569 Gerkema, T., & Zimmerman, J. T. F. (2008), *An Introduction to Internal Waves: Lecture Notes*,
570 R. Neth. Inst. for Sea Res., Den Burg.

571 Grimshaw, R., & Helfrich, K. R. (2018). Internal solitary wave generation by tidal flow over
572 topography. *Journal of Fluid Mechanics, 839*, 387-407. doi:10.1017/jfm.2018.21

573 Hamann, M. M., Alford, M. H., & Mickett, J. B. (2018). Generation and propagation of
574 nonlinear internal waves in sheared currents over the Washington continental shelf. *Journal*
575 *of Geophysical Research: Oceans*, *123*(4), 2381-2400. doi:10.1002/2017JC013388

576 Haury, L. R., Briscoe, M. G., & Orr, M. H. (1979). Tidally generated internal wave packets in
577 Massachusetts Bay. *Nature*, *278*(5702), 312-317. doi:10.1038/278312a0

578 Helfrich, K. R., & Melville, W. K. (2006). Long nonlinear internal waves. *Annual Review of*
579 *Fluid Mechanics*, *38*, 395-425.

580 Hosegood, P., Bonnin, J., & van Haren, H. (2004). Solibore-induced sediment resuspension in
581 the Faeroe-Shetland Channel. *Geophysical Research Letters*, *31*(9).
582 doi:10.1029/2004GL019544

583 Huang, W., Johannessen, J., Alpers, W., Yang, J., & Gan, X. (2008). Spatial and temporal
584 variations of internal wave sea surface signatures in the northern South China Sea studied
585 by spaceborne SAR imagery. Paper SP-656 presented at of SeaSAR 2008, Frascati, Italy,
586 21–25 January.

587 Jackson, C. R., Da Silva, J. C., & Jeans, G. (2012). The generation of nonlinear internal waves.
588 *Oceanography*, *25*(2), 108-123. doi:10.5670/oceanog.2012.46

589 Jia, T., Liang, J. J., Li, X. -M., & Sha, J. (2018). SAR observation and numerical simulation of
590 internal solitary wave refraction and reconnection behind the Dongsha Atoll. *Journal of*
591 *Geophysical Research: Oceans*, *123*(1), 74-89. doi:10.1002/2017JC013389

592 Kelly, S. M., & Nash, J. D. (2010). Internal-tide generation and destruction by shoaling internal
593 tides. *Geophysical Research Letters*, *37*(23). doi:10.1029/2010GL045598

594 Kozlov, I., Romanenkov, D., Zimin, A., & Chapron, B. (2014). SAR observing large-scale
595 nonlinear internal waves in the White Sea. *Remote Sensing of Environment*, *147*, 99-107.
596 doi:10.1016/j.rse.2014.02.017

597 Lavelle, J. W., & Thacker, W. C. (2008). A pretty good sponge: Dealing with open boundaries in
598 limited-area ocean models. *Ocean Modelling*, *20*(3), 270-292.
599 doi:10.1016/j.ocemod.2007.10.002

Lee, C. Y., & Beardsley, R. C. (1974). The generation of long nonlinear internal waves in a weakly stratified shear flow. *Journal of Geophysical Research, 79*(3), 453-462. doi:10.1029/JC079i003p00453

Li, D., Chen, X., & Liu, A. (2011). On the generation and evolution of internal solitary waves in the northwestern South China Sea. *Ocean Modelling, 40*(2), 105-119. doi:10.1016/j.ocemod.2011.08.005

Li, Q. (2014). Numerical assessment of factors affecting nonlinear internal waves in the South China Sea. *Progress in Oceanography, 121*, 24-43. doi:10.1016/j.pocean.2013.03.006

Li, X., Zhao, Z., & Pichel, W. G. (2008). Internal solitary waves in the northwestern South China Sea inferred from satellite images. *Geophysical Research Letters, 35*(13). doi:10.1029/2008GL034272

Liang, J., Li, X. -M., Sha, J., Jia, T., & Ren, Y. (2019). The lifecycle of nonlinear internal waves in the northwestern South China Sea. *Journal of Physical Oceanography*, *49*(8), 2133-2145. doi:10.1175/JPO-D-18-0231.1

Liu, A. K., Chang, Y. S., Hsu, M. K., & Liang, N. K. (1998). Evolution of nonlinear internal waves in the East and South China Seas. *Journal of Geophysical Research: Oceans, 103*(C4), 7995-8008. doi:10.1029/97JC01918

Marshall, J., Adcroft, A., Hill, C., Perelman, L., & Heisey, C. (1997a). A finite-volume, incompressible Navier Stokes model for studies of the ocean on parallel computers. *Journal of Geophysical Research: Oceans*, *102*(C3), 5753-5766. doi:10.1029/96JC02775

Marshall, J., Hill, C., Perelman, L., & Adcroft, A. (1997b). Hydrostatic, quasi-hydrostatic, and nonhydrostatic ocean modeling. *Journal of Geophysical Research: Oceans*, *102*(C3), 5733-5752. doi:10.1029/96JC02776

Maxworthy, T. (1979). A note on the internal solitary waves produced by tidal flow over a three-dimensional ridge. *Journal of Geophysical Research: Oceans, 84*(C1), 338-346. doi:10.1029/JC084iC01p00338

Nash, J. D., Kelly, S. M., Shroyer, E. L., Moum, J. N., & Duda, T. F. (2012). The unpredictable nature of internal tides on continental shelves. *Journal of Physical Oceanography*, *42*(11), 1981-2000. doi:10.1175/JPO-D-12-028.1

Nazarian, R. H., & Legg, S. (2017). Internal wave scattering in continental slope canyons, Part 2: A comparison of ray tracing and numerical simulations. *Ocean Modelling*, *118*, 16-30. doi:10.1016/j.ocemod.2017.07.005

Pacanowski, R. C., & Philander, S. G. H. (1981). Parameterization of vertical mixing in numerical models of tropical oceans. *Journal of Physical Oceanography*, *11*(11), 1443-1451. doi:10.1175/1520-0485(1981)011<1443:POVMIN>2.0.CO;2

635 Pingree, R. D., & New, A. L. (1991). Abyssal penetration and bottom reflection of internal tidal
636 energy in the Bay of Biscay. *Journal of Physical Oceanography*, 21(1), 28-39.
637 doi:10.1175/1520-0485(1991)021<0028:APABRO>2.0.CO;2

638 Quaresma, L. S., Vitorino, J., Oliveira, A., & Da Silva, J. (2007). Evidence of sediment
639 resuspension by nonlinear internal waves on the western Portuguese mid-shelf. *Marine*
640 *Geology*, *246*(2-4), 123-143. doi:10.1016/j.margeo.2007.04.019

641 Sandstrom, H., & Elliott, J. A. (1984). Internal tide and solitons on the Scotian Shelf: A nutrient
642 pump at work. *Journal of Geophysical Research: Oceans*, *89*(C4), 6415-6426.
643 doi:10.1029/JC089iC04p06415

644 Sherwin, T. J., Vlasenko, V. I., Stashchuk, N., Jeans, D. G., & Jones, B. (2002). Along-slope
645 generation as an explanation for some unusually large internal tides. *Deep Sea Research*
646 *Part I: Oceanographic Research Papers*, *49*(10), 1787-1799.

647 Shi, M. (2014). Study comments on circulation in Beibu Gulf. *Guangxi Sciences*, *21*(4), 313-324.
648 (in Chinese)

649 Su, J., & Pohlmann, T. (2009). Wind and topography influence on an upwelling system at the
650 eastern Hainan coast. *Journal of Geophysical Research: Oceans*, *114*(C6).
651 doi:10.1029/2008JC005018

652 Wang, J., Huang, W., Yang, J., Zhang, H., & Zheng, G. (2013). Study of the propagation
653 direction of the internal waves in the South China Sea using satellite images. *Acta*
654 *Oceanologica Sinica*, *32*(5), 42-50. doi:10.1007/s13131-013-0312-6

655 Xu, J., Chen, Z., Xie, J., & Cai, S. (2016). On generation and evolution of seaward propagating
656 internal solitary waves in the northwestern South China Sea. *Communications in Nonlinear*
657 *Science and Numerical Simulation*, *32*, 122-136. doi:10.1016/j.cnsns.2015.08.013

658 Xu, Z., Yin, B., Hou, Y., Fan, Z., & Liu, A. K. (2010). A study of internal solitary waves
659 observed on the continental shelf in the northwestern South China Sea. *Acta Oceanologica*
660 *Sinica*, *29*(3), 18-25. doi:10.1007/s13131-010-0033-z

661 Yan, T., Qi, Y., Jing, Z., & Cai, S. (2020). Seasonal and spatial features of barotropic and
662 baroclinic tides in the northwestern South China Sea. *Journal of Geophysical Research:*
663 *Oceans*, *125*(1). doi:10.1029/2018JC014860

664 Zeng, L., Wang, D., Chen, J., Wang, W., & Chen, R. (2016). SCSPOD14, a South China Sea
665 physical oceanographic dataset derived from in situ measurements during 1919-2014.
666 *Scientific data*, *3*. doi:10.1038/sdata.2016.29

667 Zhao, Z. (2014). Internal tide radiation from the Luzon Strait. *Journal of Geophysical Research:*
668 *Oceans*, *119*(8), 5434-5448. doi:10.1002/2014JC010014

669 Zhao, Z., Klemas, V., Zheng, Q., & Yan, X. H. (2004). Remote sensing evidence for baroclinic
670 tide origin of internal solitary waves in the northeastern South China Sea. *Geophysical*
671 *Research Letters, 31*(6). doi:10.1029/2003GL019077

672 Zheng, Q., Susanto, R. D., Ho, C. R., Song, Y. T., & Xu, Q. (2007). Statistical and dynamical
673 analyses of generation mechanisms of solitary internal waves in the northern South China
674 Sea. *Journal of Geophysical Research: Oceans*, *112*(C3). doi:10.1029/2006JC003551